PAPER

# Non-invasive pressure measurement based on magneto-mechanical effects

IOP Publishing Measurement Science and Technology
Meas. Sci. Technol. **29** (2018) 095106 (8pp) https://doi.org/10.1088/1361-6501/aad60f

# Non-invasive pressure measurement based on magneto-mechanical effects

**Zhoumo Zeng, Chengwu Zhao, Xinjing Huang, Jian Li and Shili Chen**

State Key Laboratory of Precision Measuring Technology and Instruments, Tianjin University, Tianjin, People's Republic of China

E-mail: huangxinjing@tju.edu.cn

Received 22 April 2018, revised 8 July 2018
Accepted for publication 26 July 2018
Published 14 August 2018

**Abstract**

This paper proposes and experimentally demonstrates a non-invasive pressure measurement method based on magneto-mechanical effects. The relative permeability–stress curve is obtained using the *J*–*A* force magnetic coupling model, then imported into a finite element simulation model based on the coupled multiphysics of mechanical mechanics and static magnetics. The magnetic variations versus the pressure changes at the periphery of a pressure vessel are obtained through simulations and multi-channel magnetic measurement experiments. The proposed method shows good linearity in the range of 0–3 MPa, and is more sensitive for smaller, thinner vessels. Overrange measurement can lead to saturation. Measurement points need to be carefully chosen in order to achieve the highest sensitivity and precision. The highest sensitivity achieved is $1.314 \times 10^{-5}$ T MPa$^{-1}$, and the readily available sensitivity is about $5.0 \times 10^{-6}$ T MPa$^{-1}$. The precision in many cases is better than 0.1 MPa. The repeatability errors for the three components are about 2.7% of the full scale when referred to the most sensitive component. The measurement fluctuation over 48 h is 0.1 MPa when referred to the readily available sensitivity.

Keywords: non-invasive, pressure measurement, magneto-mechanical effect, magnetic field

(Some figures may appear in colour only in the online journal)

## 1. Introduction

Pressure is an important operational parameter of pressurized vessels. The pressure in a container can rapidly increase due to incorrect operation or abnormal chemical reactions, which can affect industrial production quality and even lead to destruction and explosion. Overload-induced safety accidents can be avoided by pressure monitoring [1, 2].

Non-invasive pressure measurements without damaging the vessel structure do not degrade the safety of a pressure system. Various non-invasive pressure measurement methods have been developed over the past few years, such as the strain gauge method [3], fiber Bragg grating (FBG) method [4], capacitor-based method [5], and ultrasonic method [6]. Among these, the strain gauge method requires stringent paste quality, and the FBG method requires costly light sources and optic demodulators. The capacitor-based method has rapid dynamic response and high sensitivity, but the measurement precision is highly susceptible to circuit noise and electromagnetic interference. The ultrasonic method is most widely used for non-invasive pressure and stress measurement by measuring the sound velocity and amplitude of acoustic waves propagating in the vessel wall or the content inside. However, it also has the disadvantages of requiring strict and sophisticated deployment, coupling agent, and high bonding precision.

According to the thin-wall stress theory of pressure vessels [7], the stress inside the wall increases with the increase of internal pressure. Because of magneto-mechanical effects [8], magnetization of the wall varies under the combined effects of the internal stress and the external magnetic fields, causing the magnetic fields around the container to change. In recent years, stress measurement technology based on the magneto-mechanical effect has emerged. By applying a strong magnetization to the pressurized vessel, the wall permeability and stress state are measured [9–11]. Changes in the stress and internal pressure can be characterized according to the change

 

of the passive magnetic signals outside the container. This is a potential pressure measurement method which has the advantages of non-invasiveness, simple driving, and low cost.

Magneto-mechanical effects can be quantitatively described by the multi-axis force-magnetic coupling model. A variety of uniaxial equivalent stresses based on elastic energy theory have been defined [12–14] that can be used to simplify the multi-axis force-magnetic coupling model. The *J–A* magnetic coupling model [15] is the most widely used among these.

In this paper, a non-invasive method for vessel pressure measurement based on magneto-mechanical effects is proposed. The *J–A* magnetic coupling model is employed to analyze the relationship between the stress and the permeability. The solid mechanics module of finite element simulation software COMSOL is used to calculate the stress of the pressure vessel. The permeability at each point of the vessel wall is obtained according to the stress-permeability curve calculated by using the *J–A* model. The magnetic fields for different internal pressures in the vessel are calculated by using the magnetic field–no current module of COMSOL to obtain the magnetic field–pressure curves. A non-intrusive magnetic pressure measurement platform is thus developed. The feasibility and validation of the proposed method are fully demonstrated through theoretical analyses and experiments.

## 2. Theory of measurement

Inside ferromagnetic materials, there are many small regions of spontaneous magnetization, called magnetic domains. A magnetic domain wall is formed between two adjacent magnetic domains with different spontaneous magnetization directions. The main role of the magnetic domain wall is to achieve the transition of the magnetization directions of the two magnetic domains. Under the action of stress, the ferromagnetic material is deformed. Microscopically, the magnetic domain undergoes magnetization direction rotation or domain wall movement. Macroscopically, the internal magnetization and the equivalent magnetic permeability is changed, and the external induced magnetic fields also vary. By measuring the external magnetic field changes, it is possible to infer internal stress changes in the steel. According to the stress distribution theory of thin-walled pressure vessels, the vessel stress is linearly proportional to the internal pressure. Therefore, the internal pressure can be measured by measuring the magnetic fields near the vessel.

The measurement principle is as follows: pressure changes $p \rightarrow$ stress changes $\sigma \rightarrow$ magnetic domain changes $\rightarrow$ magnetic permeability changes $\mu_r \rightarrow$ induced magnetic field changes $B$. Before implementing the magnetic measurement scheme, the influence of differences in pressure and container size on the magnetic field distribution around the vessel needs to be analyzed using the finite element simulation, in order to demonstrate the feasibility of pressure magnetic measurements. The magneto-mechanical effect can be quantitatively described by the *J–A* magnetic coupling model, using which the $\mu_r - \sigma$ curve can be derived. The $\mu_r - \sigma$ curve can be conveniently imported into the finite element model of the force and magnetics multi-physics simulations.

Based on the *J–A* model, the effect of the stress $\sigma$ and the external magnetic field $H$ can be equivalent to an equivalent magnetic field $H_e$ [16, 17]:

$$H_e = H + \alpha M + \frac{3\sigma}{\mu_0}\left[\left(\gamma_1 + \sigma\gamma_1'\right)M + 2\left(\gamma_2 + \sigma\gamma_2'\right)M^3\right], \tag{1}$$

where $\gamma_1, \gamma_1', \gamma_2, \gamma_2'$ are magnetostrictive coefficients, $M$ is the magnetization, and $\alpha$ is the coupling parameter.

Hysteresis-free magnetization intensity $M_{an}$ is equivalent to the hysteresis-free magnetization under the effect of a magnetic field $H_e$ and 0 MPa, which is described by $M_{an}(H, \sigma) = M_{an}(H_e, 0)$, and $M_{an}(H_e, 0)$ is described as follows:

$$M_{an}(H_e, 0) = M_S\left(\coth\left(\frac{H_e}{a}\right) - \frac{a}{H_e}\right), \tag{2}$$

where $a$ is the material planning constant.

Magnetization $M$, reversible magnetization $M_{rev}$, irreversible magnetization $M_{irr}$, and hysteresis-free magnetization $M_{an}$ have a relationship as follows:

$$\begin{cases} M_{rev} = c(M_{an} - M_{irr}) \\ M = (M_{rev} + M_{irr}) \end{cases}, \tag{3}$$

and

$$\mathrm{d}M_{irr} = \frac{1}{\xi}\frac{\sigma}{E}(M_{an} - M_{irr})\,\mathrm{d}\sigma, \tag{4}$$

where $E$ is the Young's modulus, and $\xi$ is a parameter related to the energy per unit volume. The relationship between the magnetization $M$ and the stress $\sigma$ can be obtained from equations (3) and (4):

$$\frac{\mathrm{d}M}{\mathrm{d}\sigma} = \frac{\sigma}{E\xi}(M_{an} - M) + c\frac{\mathrm{d}M_{an}}{\mathrm{d}\sigma}. \tag{5}$$

The parameters are selected based on the experimental results of Craik and Wood [18, 19]. By defining the relative permeability calculation as [20]

$$\mu_r = \frac{M}{H} + 1 \tag{6}$$

and using equations (1), (2), (5), and (6), the permeability-stress ($\mu_r - \sigma$) curve is numerically calculated. The $\mu_r - \sigma$ curves with three uniaxial magnetic fields of $H = 1\ \mathrm{A\,m^{-1}}$, $H = 25\ \mathrm{A\,m^{-1}}$, and $H = 50\ \mathrm{A\,m^{-1}}$ are shown in figure 1.

Figure 1 shows that the relative permeability increases rapidly and linearly with the increase of the tensile stress, then slowly increases, reaching a maximum point when $\sigma = 121.8$ MPa. It then decreases with the increase of the stress. Similarly, the relative permeability rapidly and linearly increases with the increase of the compressive stress and then slowly increases, reaching a maximum point when $\sigma = -52.8$ MPa after which it decreases with the increase of the stress. This shows the saturation of magnetic coupling. When the material is subjected to tension or pressure, the magnetic domain walls will move and bend. The magnetization direction of the magnetic domain turns to the direction of the stress, causing an increase of magnetization. As the force

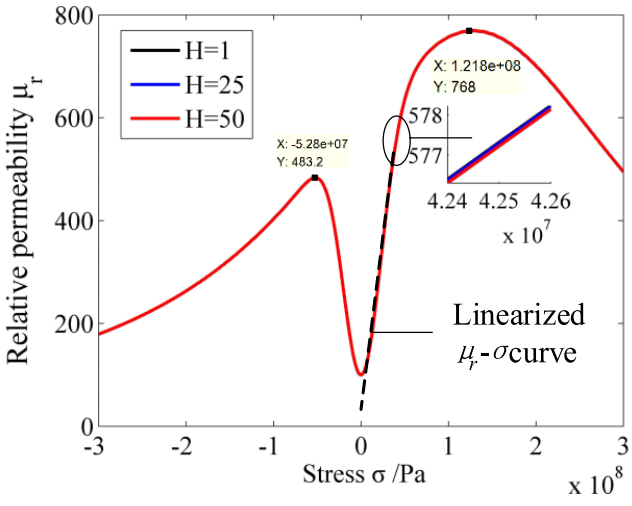


**Figure 1.** Curves of $\mu_r$ versus $\sigma$ at various values of $H$.

increases, the internal pinning effect of the material increases and the wall movement of the magnetic domain is hindered. The rate of increase of magnetization with stress rapidly decreases, and increased demagnetization results in decreased magnetization.

The linear range of the $\mu_r - \sigma$ curves for tensile stress is 0–60 MPa. When the external magnetic field is $H = 1$ A m$^{-1}$, $H = 25$ A m$^{-1}$, $H = 50$ A m$^{-1}$, there is no difference for the $\mu_r - \sigma$ curves. Considering that the three components of the geomagnetic field are all less than 50 A m$^{-1}$, the relative magnetic permeability can be considered not to be affected by external magnetic fields. This curve will be used to import the magnetic permeability of each point in the vessel wall, which is a bridge connecting the solid mechanics simulation and the magnetic field–no current simulation.

## 3. Numerical simulations

The model was built by using solid mechanics and magnetostatic modules in COMSOL, as shown in figure 2.

First, geometrically model the pressure vessel. The vessel height $h$ is 800 mm, the outer diameter $D_1$ is 275 mm, the inner diameter $D_2$ is 260 mm, and the wall thickness $\delta$ is 7.5 mm. A top cap and six bolts are also modeled to simulate the vessel used in the experiments. Second, configure the material properties. The material of the vessel is set as structural steel with the Young's modulus of $2 \times 10^9$ Pa, the Poisson's ratio of 0.3, and the density of 7850 kg m$^{-3}$. The relative permeability of the air and water domains is set to 1. The relative permeability of each point on the vessel is set to $\mu_r$, the values of which are imported via the $\mu_r - \sigma$ curve via a diagonal matrix for each component along the three coordinate axes. Third, add physics and set the boundary conditions. In the mechanical physics, a fixed constraint is applied on the bottom surface of the vessel, and the pressure is applied on the inner surface to cause stress distributions on the vessel wall. In the magnetostatic physics, the vessel is covered with air, and an ambient magnetic field of $\mathbf{H} = (Hx, Hy, Hz) = (28, 28, 0)$ A m$^{-1}$ applied in all domains. Fourth, mesh and compute. All the domains are meshed into 140 850 free triangular elements.

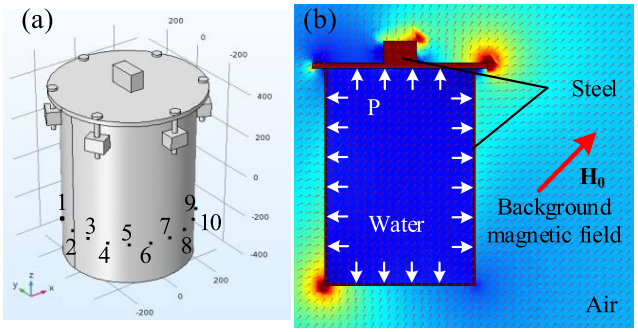


**Figure 2.** Simulation model.

The numbers of vertex, edge, and boundary elements are 154, 1584 and 17 954. Minimum element quality is 0.096 73. Then, the magnetic fields in all the domains are calculated.

Because of a low pressure measurement range, 0–3 MPa in the experiment and 0–5 MPa in the simulation, the maximum stress in the vessel is no more than 50 MPa. It is far less than both the saturation stress (121.8 MPa) of the $\mu_r - \sigma$ curve and the yield stress of the structural low-carbon steel (>200 MPa). Therefore, a linear elastic model is used for simulations; the geometric non-linearity in the mechanics is not considered in this paper.

Points 1 to 10 are observation points of the magnetic fields in the simulation. The radial, circular, and axial magnetic flux density components, $B_r$, $B_c$, and $B_a$, are calculated as $B_r = B_x \cos\theta + B_y \sin\theta$, $B_c = B_x \sin\theta - B_y \cos\theta$, $B_a = B_z$, where $\theta$ is the angle between the $x$ axis and the line from the origin to the observation point, and $B_x$, $B_y$, and $B_z$ are the magnetic flux density components in the Descartes coordinate system.

### 3.1. Measurement range

Using the model that has been built, the simulations about the variation characteristics of the magnetic fields induced by the pressurized vessel along with the internal pressure were carried out. The results are shown in figure 3. Figures 3(a)–(c) are simulation results when importing the $\mu_r - \sigma$ curve using the original *J–A* model. It can be seen that there is a flat part at the beginning of the curve, which is inconsistent with the results of the later experimental measurements. Therefore, linear correction of the $\mu_r - \sigma$ curve for the original *J–A* model is performed, as shown by the dashed line in figure 1. Figures 3(d)–(f) are corrected simulation results, and are consistent with the results of the later experiments. The magnetic fields at different points increase or decrease monotonously with the increase of the pressure. As the magnetic field has a tendency to saturation, the available measurement range lies in the low pressure section. In the high pressure section, the sensitivity is close to 0 due to saturation.

In order to validate the assumption that such a magnetic saturation is not exclusive to the tested vessel, the simulation of sweeping the permeability of a steel plate in an ambient magnetic field was carried out. The induced magnetic field near a steel plate as a function of the permeability is shown in figure 4. It can be seen that similar saturation does exist for the

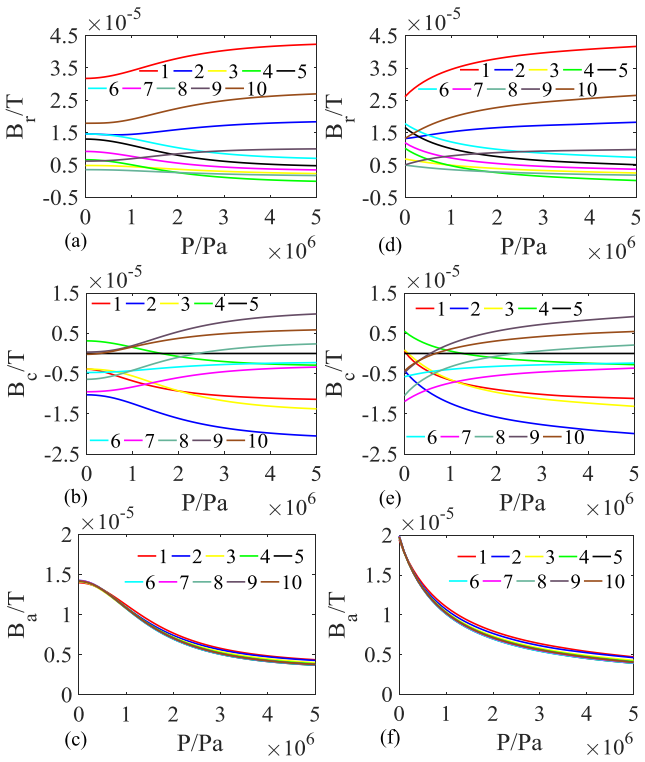


**Figure 3.** Curves of the magnetic fields versus pressure at each measuring point, (a)–(c) using the original $\mu_r - \sigma$ curve, (d)–(f) using the linearly modified $\mu_r - \sigma$ curve.

steel plate, and the saturation appears after the permeability is larger than 500. However, as shown in figure 1, when $\mu_r$ is around 500, the $\mu_r - \sigma$ curve is still linear and has not reached its saturation point. This indicates that the saturation disadvantage of the proposed pressure measurement method is not induced by the magneto-mechanical effect, but is simply due to an excessive magnetic permeability.

### 3.2. Influences of vessel sizes

Using the linear modified $\mu_r - \sigma$ curve, simulation analyses were performed for pressurized vessels of various sizes. Figure 5(a) shows the simulation results for three pressure vessels with different heights and diameters, but with the same diameter–thickness ratio. Figure 5(b) shows the simulation results for three pressure vessels with different thicknesses, but with the same height and diameter. A point outside the pressure vessel was selected for the analyses. For ease of comparison, each curve has had its own initial value subtracted. It can be seen that for the same diameter–thickness ratio, the smaller the pressure vessel size is, the more sensitive the magnetic field is to the pressure change; for the same diameter, the thinner the pressure vessel is, the more sensitive the magnetic field is to the pressure change. This is reasonable since the stress is more sensitive to the internal pressure for a thinner and smaller container with the same internal pressure, and the magnetic field is also more sensitive to the internal pressure.

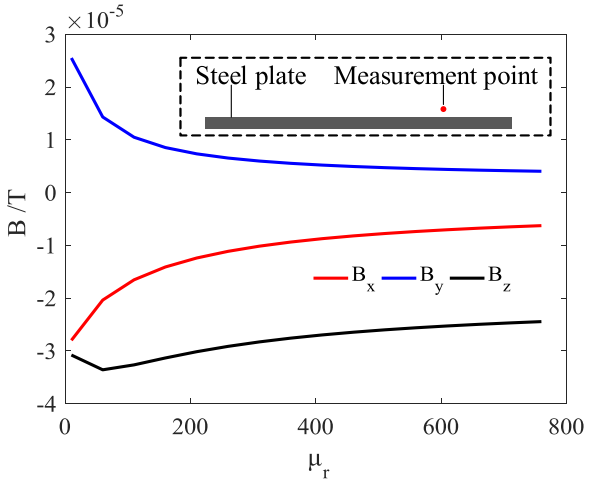


**Figure 4.** Induced magnetic field as a function of permeability for a steel plate.

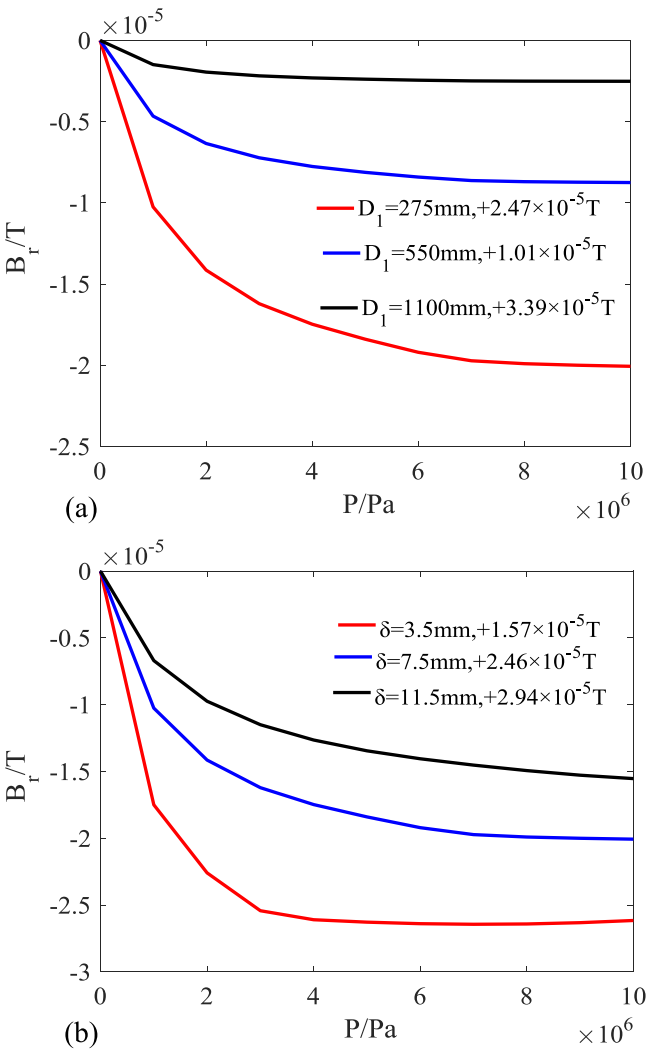


**Figure 5.** Effects of vessel size on the magnetic field-pressure curves: (a) different profile size; (b) different wall thickness.

## 4. Experiments

Figure 6 shows the experimental method and apparatus. Figure 6(a) is the schematic diagram of the experimental

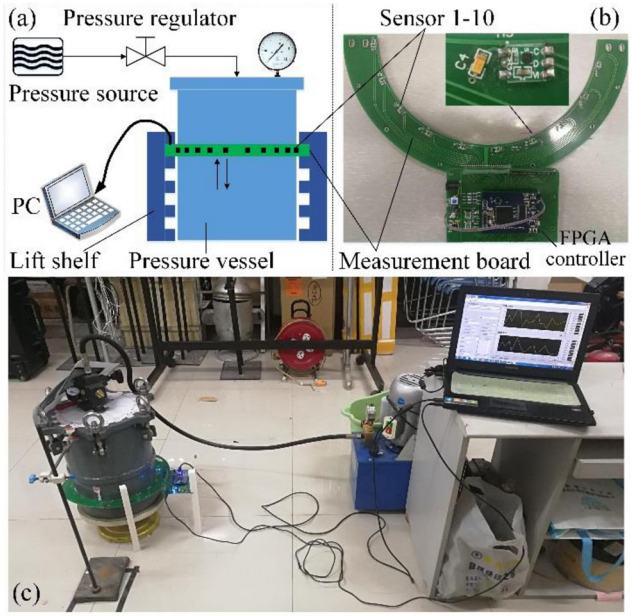


**Figure 6.** Experiments: (a) schematic of measurements; (b) measuring device; (c) experimental photograph.

platform, and figure 6(b) is the measuring device. The magnetic signal acquisition, recording, and display device used during the experiment is self-designed and developed. The device includes an annulus base board, ten anisotropic magneto-resistive sensors, and an FPGA controller. The magnetic sensors are soldered onto the base board. The magnetic sensors are circularly and evenly distributed on the measuring circuit along the wall of the vessel. The sensors can measure the magnetic fields in three directions: the radial, circular, and axial magnetic flux density components around the vessel, $B_r, B_a, B_c$. The FPGA controller is connected to the base board and the host computer. The FPGA controller synchronously collects the magnetic signals of all the sensors via IIC bus and transmits them to the host computer through USB for saving and display.

The pressure source is used to pressurize the pressure vessel. The final pressure is controlled by the pressure regulator. A high-precision pressure gauge is used to display the pressure in real time. Two lifting frames are used to adjust the height of the measuring device and sensors when searching the measurement plane that has high sensitivity. For ease of operation, the vessel is pressurized up to 3 MPa and then decompressed to 0 MPa for all the magnetic pressure measurement experiments. Operational procedure is as follows: use the pressure source to pressurize the vessel until the pressure is 3 MPa; start the measuring device and host computer; decrease the pressure inside the vessel through the pressure regulator; record and display the changing magnetic signals on the computer; and finally, stop the measuring device when the pressure is 0 MPa. There are three groups of experiments to be undertaken: (1) select measuring points with high sensitivities via one-time pressure release; (2) sensitivity test via step-by-step pressure release; (3) repeatability and stability test.

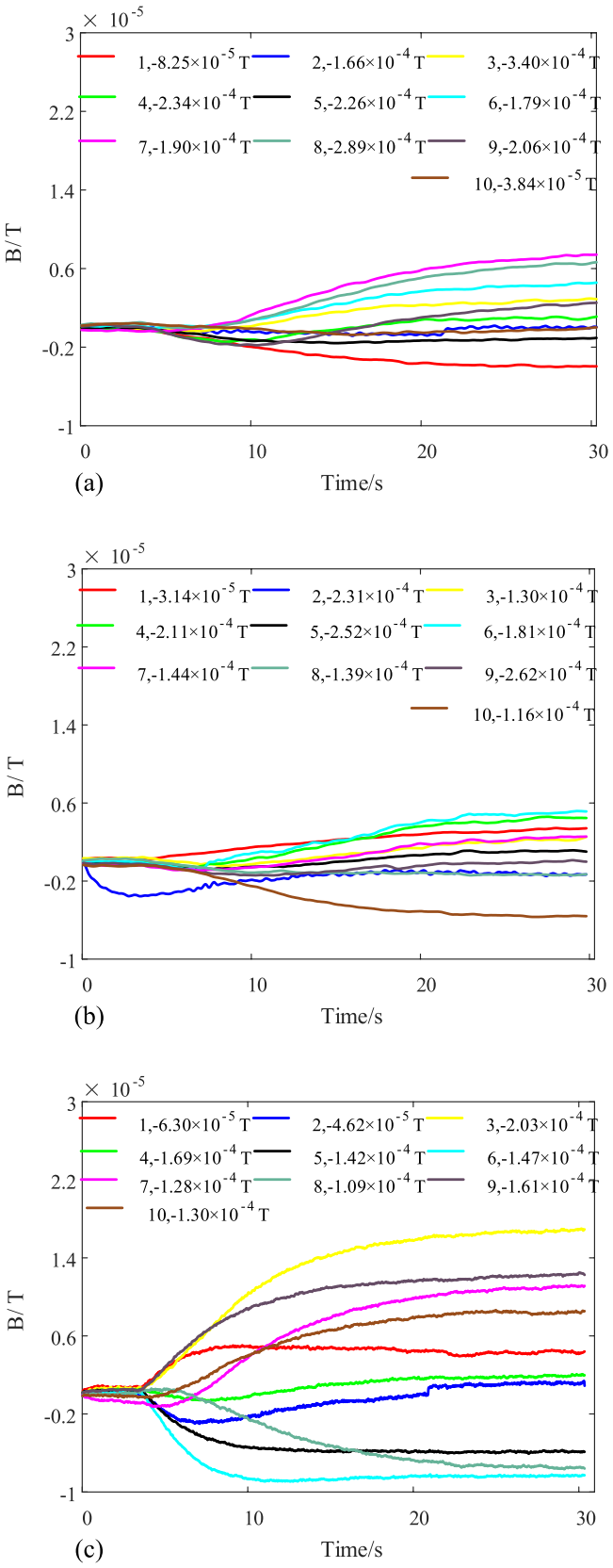


**Figure 7.** Sensitivity comparison of pressure measurements at various heights.

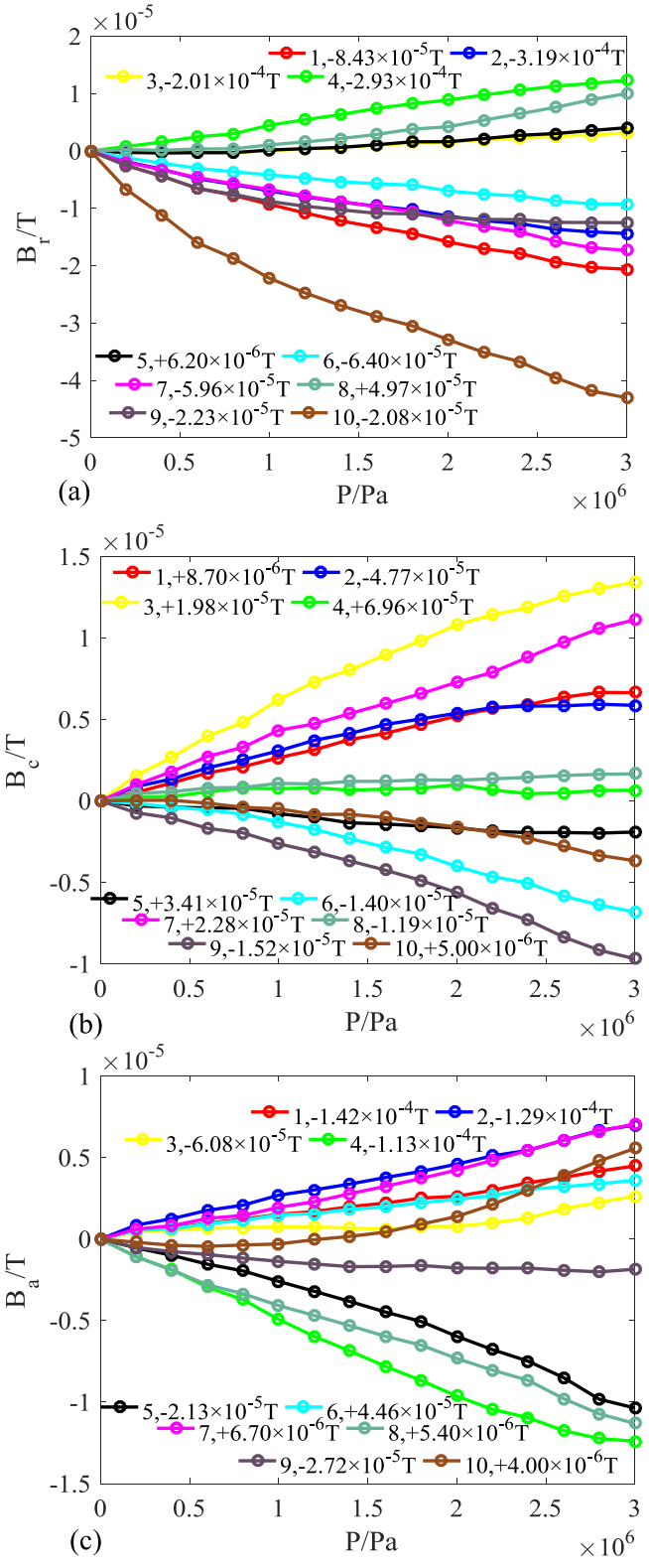


**Figure 8.** Pressure measurement results at the lower position with an adjustment interval of 0.2 Mpa.

## 5. Results and discussions

### *5.1. Selection of measuring points*

Due to the complex structure of the pressure vessel in the experiments, including fastening bolts, caps, and welds, the magnetic fields around the curve are not so smooth and uniform as in the simulation. Therefore, measurement points need to be carefully selected for high sensitivity. The magnetometers were fixed at three different heights, and rapid pressure relief tests were performed in order to select the location with higher sensitivity. This pressure relief was accomplished by opening the regulator valve and continuously leaking water. The pressure range is 0–3 MPa.

**Table 1.** Sensitivity and precision when using $B_r$.

| Sensor | $e_m$ $\times10^{-7}$ T | $\bar{e}$ $\times10^{-7}$ T | Sensitivity $\times10^{-7}$ T MPa$^{-1}$ | Precision $\times10^{-6}$ Pa |
|---|---|---|---|---|
| 1 | 19.1 | 6.4 | −67.4 | −0.095 |
| 2 | 16.2 | 5.8 | −46.7 | −0.124 |
| 3 | 8 | 2.5 | 12.1 | 0.207 |
| 4 | 6.5 | 2.6 | 43.1 | 0.060 |
| 5 | 10.1 | 3.5 | 14.9 | 0.235 |
| 6 | 8.9 | 2.7 | −29.7 | −0.091 |
| 7 | 8.7 | 2.6 | −56.2 | *−0.046* |
| 8 | 16.1 | 7.8 | 33.7 | 0.231 |
| 9 | 34.9 | 12.8 | −37.0 | *−0.346* |
| 10 | 62.3 | 18.1 | *−131.4* | −0.138 |
| Average | 19.1 | 6.5 | | |

Figure 7 shows the results of rough sensitivity tests at various heights. Figure 7(a) is the result obtained near the cap, figure 7(b) is the result obtained at the position a little farther away from the cap, and figure 7(c) is the result near the bottom. It can be seen that magnetic fields of the ten measuring points near the bottom change more significantly with the pressure change than that at the other two heights. The measuring points should be chosen near the bottom or in the lower part of the container in order to achieve a high sensitivity.

The sensor array is located in the lower part of the pressure vessel and the magnetic variation of each channel versus the pressure in the range of 0–3 MPa measured. The way to change the pressure here is not a free continuous relief. Instead, the pressure is adjusted via the pressure regulator with an interval of 0.2 MPa, and each pressure is kept for a couple of seconds. The magnetic signal corresponding to each pressure during this period of time is then averaged as the magnetic signal corresponding to the pressure. The results are shown in figure 8.

For ease of comparison, the curve obtained at each measurement point has had its own initial value subtracted. It can be seen that the magnetic field changes at most measuring points have an approximately linear relationship with the pressure changes. This is consistent with the simulation results. Both the experimental and simulation results prove the feasibility of pressure measurement by monitoring the changes of the magnetic fields around a pressure vessel. The differences between the initial values of different points are large, indicating that casually moving the measuring points is not allowable in pressure measurements. The relative, rather than absolute, value of the magnetic field can be used to indicate the vessel pressure, because of the complex original magnetizations and the induced field superpositions of the vessel.

**Table 2.** Sensitivity and precision when using $B_c$.

| Sensor | $e_m$ $\times 10^{-7}$ T | $\bar{e}$ $\times 10^{-7}$ T | Sensitivity $\times 10^{-7}$ T MPa$^{-1}$ | Precision $\times 10^{-6}$ Pa |
|---|---|---|---|---|
| 1 | 6.3 | 1.7 | 23.3 | *0.073* |
| 2 | 10.5 | 4.3 | 20.3 | 0.212 |
| 3 | 12.1 | 5.3 | 44.7 | 0.119 |
| 4 | 4.1 | 1.9 | *1.2* | *1.583* |
| 5 | 3.5 | 1.3 | −7.1 | −0.183 |
| 6 | 7.5 | 3 | −24.2 | −0.124 |
| 7 | 4.2 | 1.6 | 35.8 | 0.045 |
| 8 | 4 | 1 | 4.6 | 0.217 |
| 9 | 5.4 | 3.3 | −32.3 | −0.102 |
| 10 | 5.6 | 2.5 | −12.3 | −0.203 |
| Average | 6.3 | 2.6 | | — |

**Table 3.** Sensitivity and precision when using $B_a$.

| Sensor | $e_m$ $\times 10^{-7}$ T | $\bar{e}$ $\times 10^{-7}$ T | Sensitivity $\times 10^{-7}$ T MPa$^{-1}$ | Precision $\times 10^{-6}$ Pa |
|---|---|---|---|---|
| 1 | 2.5 | 1.0 | 14.1 | 0.071 |
| 2 | 2.9 | 1.1 | 22.1 | 0.050 |
| 3 | 7.1 | 3 | 6.3 | *0.476* |
| 4 | 10.8 | 3.4 | −43.5 | −0.078 |
| 5 | 7.7 | 3.6 | −34.5 | −0.104 |
| 6 | 1.9 | 0.6 | 11.5 | 0.052 |
| 7 | 3.9 | 2.1 | 23.5 | 0.089 |
| 8 | 3.3 | 1.8 | −36 | *−0.050* |
| 9 | 5.9 | 1.8 | −5.4 | −0.333 |
| 10 | 15.3 | 7.5 | 18.8 | 0.399 |
| Average | 6.1 | 2.6 | | |

### 5.2. Sensitivity and precision

The sensitivity of magnetic-based pressure measurement depends on which magnetic component is employed and where the sensor is deployed. Linear fitting was done for each of the 30 measurement curves in figure 8 of the three components in order to obtain and analyze the deviation, sensitivity, and precision. The results are listed in tables 1–3. $e_m$ and $\bar{e}$ are the maximum and average of the deviations between the measure values and the fitting values, respectively. Precision is calculated by using $\bar{e}$/Sensitivity for each sensor and its component.

It can be seen that for the current measurements, the sensitivity and precision of different measurement points are different due to the randomness of the magnetic measurement errors. The average measurement errors of the induced magnetic signals for the three components are all close to or less than $5 \times 10^{-7}$ T. The maximum errors are approximately $1.0 \times 10^{-6}$ T. The sensitivity when using $B_r$ is higher than using $B_c$ and $B_a$. The precisions for the three components are similar in terms of their respective highest and lowest precisions, as underlined in the last columns of tables 1–3.

The highest sensitivity of $1.314 \times 10^{-5}$ T MPa$^{-1}$ is achieved by the radial component of the 10th sensor, while the lowest sensitivity of $1.2 \times 10^{-7}$ T MPa$^{-1}$ occurs at the circular component of the 4th sensor. The highest sensitivity is 110 times the lowest one. The highest precision of −0.046 MPa is achieved by the radial component of the 7th sensor, not the one with the highest sensitivity. Many of the precisions are better than 0.1 MPa, and the highest precision is 0.046 MPa. Low precision is generally accompanied by low sensitivity.

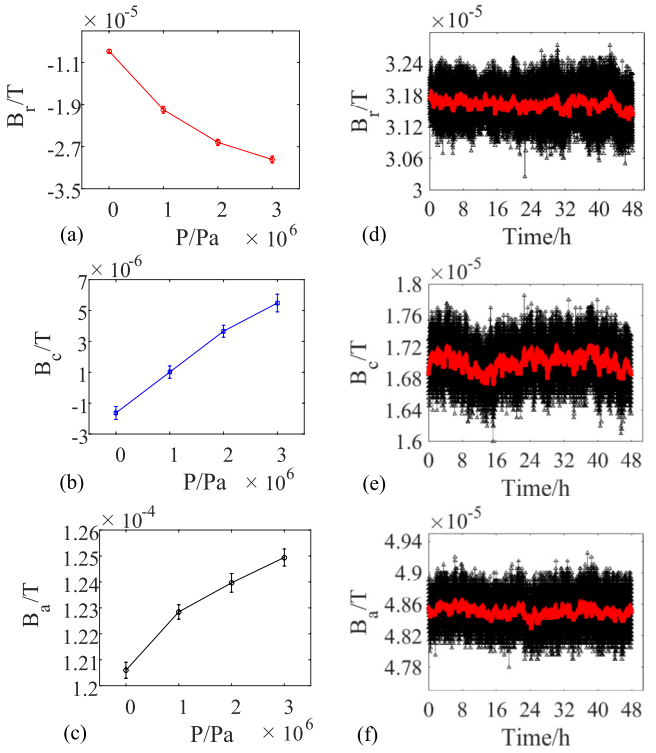


**Figure 9.** Repeatability and stability demonstrations.

### 5.3. Repeatability and stability

In order to verify the measurement repeatability of the proposed method, the data from all the channels were collected in the morning and afternoon for seven consecutive days. At the same time, the experimental conditions such as the position and posture of the pressure vessel and the sensors were left unchanged. The average and variance of the 14 groups of data were calculated, and the results are shown in figures 9(a)–(c). It can be seen that the magnetic field for the same pressure is repeatable and concentrated around one value. $B_r$ has the highest sensitivity among the three components. The repeating errors for the three components are all about $6 \times 10^{-7}$ T , which is about 2.7% of the full scale if referred to $B_r$, $2.7\% = 6 \times 10^{-7}$ T/$2.2 \times 10^{-5}$ T.

The stability of the magnetic field is a precondition for its being employed to measure the pressure. Therefore, the stability of the magnetic signal at one point near the pressure vessel was measured for 48 h, as shown in figures 9(d)–(f). The black curve represents the original raw data, and the red curve represents the data processed by using the zero-phase filter. Considering that the pressure change of an on-site vessel is relatively slow, so the smoothing the measurements over a couple of seconds is allowable and desirable and can improve the measurement accuracy. It can be seen that the amount of magnetic field fluctuation over 48 h is only $5 \times 10^{-7}$ T, of which the equivalent precision is 0.1 MPa for the sensitivity

of $5 \times 10^{-6}$ T MPa$^{-1}$, which is approximately the average of the sensitivity in table 1. Therefore, it is reliable to use the induced magnetic field to measure the vessel pressure.

## 6. Conclusions

This paper proposes and demonstrates a non-invasive pressure measurement method based on magneto-mechanical effects. The relationship between the stress and the relative permeability is established by using the *J–A* force magnetic coupling model, and the variations of the magnetic fields with the pressure changes at the periphery of the pressure vessel are obtained through simulations and experiments. The change of pressure inside the pressure vessel can noticeably affect the magnetic fields at the periphery of the pressurized vessel. The proposed method is demonstrated to be suitable for the low pressure range of 0–3 MPa, and is more sensitive for a smaller and thinner vessel. Overrange measurement can lead to saturation.

The sensitivity and precision of different measurement points are different due to the complex original magnetizations and the induced field superpositions of the vessel. The magnetic variations surrounding the pressure vessel are measured in the range of 0–3 MPa. Among these measurements, the highest sensitivity achieved is $1.314 \times 10^{-5}$ T MPa$^{-1}$, and the readily available sensitivity is about $5 \times 10^{-6}$ T MPa$^{-1}$. Many of the precision values are better than 0.1 MPa. The repeatability errors for the three components are about 2.7% of the full scale when referred to the most sensitive component. The measurement fluctuation over 48 h is 0.1 MPa when referred to the readily available sensitivity.

However, at present, this method is feasible and reliable for the pressure measurement of a fixed vessel located in a stable magnetic environment. It requires further effort to overcome the disadvantage of being susceptible to variance in the posture and position of the pressure vessel, and to ambient magnetic variances.

## Acknowledgments

This work was supported by National Natural Science Foundation of China (Nos 51604192, 61773283, and 61473205).

## ORCID iDs

Xinjing Huang https://orcid.org/0000-0002-8964-8502

## References

[1] Huang J P 2012 Statistical analysis of special equipments in 2011 *China Spec. Equip. Saf.* **28** 37–40
[2] Li Y J, Xue W and Hu B B 2016 Research on common problems and countermeasures in chemical safety production *Manage. Sci. Technol. Small Medium-Sized Enterprises* **8** 11–2
[3] Sadeghioon A M *et al* 2016 Wireless sensor network based pipeline failure detection system using non-intrusive relative pressure and differential temperature measurements *Int. Conf. on Smart Infrastructure and Construction* pp 2–7
[4] Dong N *et al* 2017 Pressure and temperature sensor based on graphene diaphragm and fiber Bragg gratings *IEEE Photonics Technol. Lett.* **30** 431–4
[5] Liu S Y, Lu J G and Shieh H P D 2018 Influence of permittivity on the sensitivity of porous elastomer-based capacitive pressure sensors *IEEE Sens. J.* **18** 1870–6
[6] Lin W B 2017 Research on pressure measurement model based on ultrasonic wave *Master's Thesis* Zhejiang University
[7] Liu H 1987 *Plate Shell Theory* (Zhejiang: Zhejiang University Press) pp 243–71
[8] Jiles D C 1999 Theory of the magnetomechanical effect *J. Phys. D: Appl. Phys.* **28** 1537
[9] Kouli M E and Giannakis M 2016 Stress state evaluation in low carbon and TRIP steels by magnetic permeability *Materials Science and Engineering Conf. Series* p 012013
[10] Vourna P *et al* 2017 Dependence of magnetic permeability on residual stresses in welded steels *IEEE Trans. Magn.* **53** 1–4
[11] Kim J *et al* 2018 Measurement of residual stress using linearly integrated GMR sensor arrays *J. Mech. Sci. Technol.* **32** 623–30
[12] Schneider C S and Richardson J M 1982 Biaxial magnetoelasticity in steels *J. Appl. Phys.* **53** 8136–8
[13] Pearson J *et al* 2000 Biaxial stress effects on the magnetic properties of pure iron *IEEE Trans. Magn.* **36** 3251–3
[14] Zhao J, Gao M and Wang S 2009 An equivalent stress for the influence of multiaxial stress on the magnetic behavior *J. Appl. Phys.* **105** 07A313
[15] Li J W 2012 Theoretical and experimental research on magneto-mechanical effects of ferromagnetic materials under weak magnetic field *PhD Thesis* Harbin Institute of Technology
[16] Kaminski D A *et al* 1992 Angular dependence of the magnetic properties of polycrystalline iron under the action of uniaxial stress *J. Magn. Magn. Mater.* **1** 382–4
[17] Li L and Jiles D 2004 A new approach to the magnetomechanical effect *J. Appl. Phys.* **95** 7058–60
[18] Craik D J and Wood M J 1970 Magnetization changes induced by stress in a constant applied field *J. Phys.* **3** 1009–16
[19] Sablik M J and Jiles D C 1993 Coupled magnetoelastic theory of magnetic and magnetostrictive hysteresis *IEEE Trans. Magn.* **29** 2113–23
[20] Guo Y C 2014 *Ferromagnetics* (Beijing: Peking University Press) pp 8–11